Nano Energy 78 (2020) 105194

Contents lists available at ScienceDirect

Nano Energy

journal homepage: http://www.elsevier.com/locate/nanoen

Optimizing the structure of layered cathode material for higher electrochemical performance by elucidating structural evolution during heat processing

Zhongyuan Huang [a,1], Mihai Chu [a,1], Rui Wang [a,1], Weiming Zhu [a], Wenguang Zhao [a], Chaoqi Wang [a], Yanjun Zhang [a], Lunhua He [b,d,e], Jie Chen [c,d], Sihao Deng [c,d], Longwei Mei [c,d], Wang Hay Kan [c,d], Maxim Avdeev [f,g], Feng Pan [a], Yinguo Xiao [a,*]

[a] School of Advanced Materials, Peking University, Shenzhen Graduate School, Shenzhen, 518055, China
[b] Institute of Physics, Chinese Academy of Sciences, Beijing, 100190, China
[c] Institute of High Energy Physics, Chinese Academy of Sciences, Beijing, 100049, China
[d] Spallation Neutron Source Science Center, Dongguan, 523803, China
[e] Songshan Lake Materials Laboratory, Dongguan, 523808, China
[f] Australian Nuclear Science and Technology Organization, Lucas Heights, New South Wales, 2234, Australia
[g] School of Chemistry, The University of Sydney, Sydney, 2006, Australia

ARTICLE INFO

Keywords:
Layered cathode material
Neutron diffraction
Thermal stability
Li/Ni disordering
Phase transition

ABSTRACT

Improving electrochemical performance of cathode materials for lithium-ion batteries requires comprehensive understanding of their structural properties which could facilitate or impede the diffusion of lithium during charge-discharge. In order to optimize the structure and improve the electrochemical performance of layered cathode material, the detailed structural evolution as a function of heat treatment temperature in $LiNi_{0.8}Co_{0.1}Mn_{0.1}O_2$ was investigated by *in-situ* and *ex-situ* neutron powder diffraction methods. We show that both cycling stability and rate performance of $LiNi_{0.8}Co_{0.1}Mn_{0.1}O_2$ can be improved by performing heat treatment at 400 °C, which is attributed to the optimization of surface structure and the enlargement of c/a ratio. Heat treatment of $LiNi_{0.8}Co_{0.1}Mn_{0.1}O_2$ at higher temperature induces a layered-to-rock-salt structure phase transition accompanied with the precipitation of lithium oxide. A 3D phase diagram, which correlates the high temperature phases and room temperature phases, is constructed. The presentation of comprehensive phase diagrams up to 1000 °C could provide the basis for further research on not only synthesis strategy but also thermal stability in Ni-rich layered cathode materials.

1. Introduction

The development of electronic devices strongly relies on the extensive use of energy-storage technology. Nowadays, lithium-ion batteries (LIBs) are considered as dominating rechargeable energy-storage system to realize the storage and release of electrical energy for portable electronics, such as cell phones, laptop computers and so on [1,2]. Besides, LIBs are increasingly used in electric vehicles as electrical propulsion to replace propulsion by traditional fossil fuels. However, significant enhancements in energy density, cycling life and safety characteristics of LIBs are required for successful and extensive application of them as reliable power source for electric vehicles.

As the main components of LIBs, cathode materials determine the energy density and restrict the performance of LIBs [3–5]. $LiCoO_2$ with layered structure is the most used cathode material for commercial LIBs. However, the commercial $LiCoO_2$ cathode possesses limited capacity (~160 $mAh{\cdot}g^{-1}$) and poor structural stability at high charge state (>4.3 V). As a result, high-Ni cathode materials, whose chemical formula could be written as $LiNi_xCo_yMn_zO_2$ (with $x > 0.5$, $x + y + z = 1$), have attracted considerable attention due to their higher capacity (~180 $mAh{\cdot}g^{-1}$), larger energy density (~280 $Wh{\cdot}kg^{-1}$ for pouch cells) as well as the lower cost [6–8]. Nevertheless, high-Ni content also leads to two

* Corresponding author.
E-mail address: y.xiao@pku.edu.cn (Y. Xiao).
[1] These authors contributed equally to this work.

https://doi.org/10.1016/j.nanoen.2020.105194
Received 1 June 2020; Received in revised form 3 July 2020; Accepted 11 July 2020
Available online 11 August 2020

serious problems, i.e. cycling instability resulting from electrolyte reaction on the high-catalytic-activity surface at high voltage [9] and thermal instability resulting from layer-to-rock-salt transformation [10–12]. Such weaknesses inevitably shorten the cycling life of cathode and raise safety concerns [13,14].

In order to gain insight into the intrinsic origin of structural instability in high-Ni layered cathode materials and to explore the effective approach like cation doping or surface coating to improve their electrochemical performance, it is necessary to take great efforts to reveal the structural details. A systematic study on the thermal behavior, especially the evolution of structure with temperature variation, is of great significance in order to formulate strategy in modifying and optimizing the structure of high-Ni layered materials for better performance. According to previous work done using X-ray diffraction and mass spectroscopy techniques, the thermal-induced phase transformations are observed in delithiated $LiCoO_2$, $LiNi_{0.33}Co_{0.33}Mn_{0.33}O_2$, $LiNi_{0.5}Co_{0.3}Mn_{0.2}O_2$, $LiNi_{0.6}Co_{0.2}Mn_{0.2}O_2$ and $LiNi_{0.8}Co_{0.1}Mn_{0.1}O_2$ as well [15–20]. However, some important structural information associated with structural properties, such as cation mixing [21–23], lithium and oxygen loss [24] as well as their influence on electrochemical performance [25], has not been systematically explored and analyzed in detail. Due to the low sensitivity of X-ray to light elements, such as Li and O, it is difficult to deduce accurate structural information, especially the concentration of Li/Ni disordering in LIBs cathode materials by applying conventional X-ray diffraction method. In contrast, neutron can act as effective probe to determine accurate position of light elements because of its high sensitivity to nuclei of lithium and oxygen. Furthermore, neutrons can also be used to distinguish Ni, Mn, and Co since the neutron scattering lengths of these transition metals are quite different, i.e. 10.3, −3.73, and 2.49 fm, respectively. Therefore, the neutron powder diffraction (NPD) is considered as a method of choice to trace the thermal treatment induced structure changes as well as the Li and O loss in high-Ni layered cathode with increasing temperature.

Herein we focus on Ni-rich layer-structured $LiNi_{0.8}Co_{0.1}Mn_{0.1}O_2$ (labeled as NCM811) and perform systematic investigations on the structural evolution of NCM811 at pristine state during heating process. Considering that both surface and bulk structures of NCM811 will inevitably change during the heating process and lead to the change in electrochemical performance accordingly, we separately applied *in-situ* approach [26] to detect the crystal structure of NCM811 samples at certain temperature and *ex-situ* approach to investigate the modified structure after cooling down to room temperature. Combining electrochemical data and structural data, we found that heat treatment of NCM811 at temperature of ~400 °C is beneficial for NCM811 to enlarge the lithium layer spacing and modify surface morphology, resulting in the improvement of the cycling and rate performance of materials. In contrast, the heat treatment at higher temperature is detrimental to the electrochemical performance of materials due to the generation of more Li/Ni disordering and the decomposition of layered structure. Based on the *in-situ* and *ex-situ* neutron diffraction results in temperature range from room temperature to 1000 °C, we established a 3D temperature-phase fraction diagram of NCM811, which clearly demonstrates the correlation between high temperature phases and room temperature phases. Our findings not only clarify the structure evolution of NCM811 cathode material but also demonstrate that heat treatment at appropriate temperature could be a simple and effective strategy to improve the electrochemical performances of cathode materials. Our study can serve as a guide to synthesis of layered cathode materials with better capacity and safety characteristics and further development of cathode materials.

2. Experimental section

2.1. Preparation of $Ni_{0.8}Co_{0.1}Mn_{0.1}(OH)_2$ precursor

The co-precipitation method was selected to synthesize the hydroxide precursor of NCM811. Firstly, appropriate amount of $NiSO_4{\cdot}6H_2O$, $CoSO_4{\cdot}7H_2O$ and $MnSO_4{\cdot}5H_2O$ with stoichiometric ratio 8:1:1 were dissolved in deionized water. The concentration of the solution was 2.0 mol/L. Then the mixed solution was transferred into a three-necked flask with continuous stirring under N_2 atmosphere. In the meantime, 4.0 mol/L NaOH solution (aq.) and adequate amount of NH_4OH solution (aq.) as a chelating agent were gradually pumped into the flask. Maintaining stirring speed at 600 rpm, temperature at 55 °C, and pH at 10 for 8 h, the precursor powders were finally obtained through filtering, washing and drying at 100 °C in a vacuum oven overnight. It is worth noting that the powders were washed several times until the pH of the filtrate was adjusted to 7.

2.2. Preparation of NCM811 samples under different heating conditions

The dried precursor and $LiOH{\cdot}H_2O$ were mixed with molar ratio 1:1.05 and milled for 30 min. Then the mixture was transferred into a tube furnace. It was sintered at 480 °C for 8 h to guarantee the melting of LiOH and subsequently at 750 °C for 15 h to ensure sufficient reaction. The furnace atmosphere was O_2 flow and the heating rate was 3 °C/min. After cooling naturally, the as-prepared NCM811 powders were collected and divided into several parts with equal mass for further heat treatment experiments.

The thermal stability of NCM811 was investigated by tracing the structural evolution of sample under reheating process. NCM811 samples were reheated at 400, 600, 700, 800, 900 and 1000 °C, respectively for 6 h under Ar atmosphere. The heating rate was kept at 3 °C/min and all samples were cooled down to room temperature (~25 °C) with cooling rate of 3 °C/min. Once the reheating process was finished, each sample was air-tight sealed and shortly after that characterized by *ex-situ* NPD, X-ray diffraction (XRD), scanning electron microscopy (SEM), and other techniques. In addition, an as-prepared NCM811 sample was used for the *in-situ* NPD measurement by heating up to selected temperature points.

2.3. Structural characterization

The *in-situ* NPD experiments were carried out on high-resolution neutron powder diffractometer ECHIDNA in OPAL (Open Pool Australian Light Water) research reactor at ANSTO (Australian Nuclear Science and Technology Organization). A Ge(335) monochromator was used to produce a monochromatic neutron beam of wavelength 1.6215 Å. Data were collected in the 2θ range of 4°–164° with a step of 0.125°. The NCM811 sample was placed in a platinum holder to avoid unexpected reaction at high temperature, and then placed in a high temperature furnace. The first data set was collected at room temperature. Then the data were collected at 600, 700, 800, 900 and 1000 °C with the heating rate of 10 °C/min between the points. All data were collected only if the furnace temperature was stabilized at each specific temperature points. All *in-situ* neutron diffraction patterns were refined by the Rietveld method with Fullprof program [27].

The *ex-situ* NPD experiments were performed on GPPD (General Purpose Powder Diffractometer), a time-of-flight (TOF) diffractometer at China Spallation Neutron Source (CSNS), Dongguan, China. Each sample was loaded into a vanadium can with 9.1 mm diameter and the diffraction pattern was collected with wavelength ranging from 0.1 Å to 4.9 Å at room temperature under vacuum. The Rietveld refinement was used to analyze crystal structures by the Fullprof program. It is worth noting that high counting statistics and perfect peak profile [28,29] make it possible to fit the whole patterns properly with Pseudo-Voigt peak function, leading to reliable refinement results on crystal structures.

The XRD patterns were obtained by using the Bruker D8 Advance diffractometer with Cu K_α (a mixture of $\lambda_1 = 1.5406$ Å and $\lambda_2 = 1.5444$ Å) radiation. All XRD patterns were refined together with *ex-situ* NPD patterns by a combination refinement method. Morphologies of

NCM811 particles were observed by using the ZEISS Supra 55 field-emission SEM with 5 kV voltage and the JEOL-3200FS field-emission transmission electron microscopy (FE-TEM) with 300 kV accelerating voltage. The O 1s, Ni 2p and Li 1s X-ray photoelectron spectra (XPS) of all samples were obtained by an ESCA Lab 220I-XL XPS system with a focused monochromatic Al *Kα* X-ray (1486.7 eV) source. All spectra were calibrated by the C 1s peak at 284.8 eV.

2.4. Electrochemical measurements

The NCM811 cathode samples were prepared from the composite slurry with 80 wt% tested samples as active material, 10 wt% acetylene black as conductive additives and 10 wt% polyvinylidene fluoride (PVDF) dissolved in N-methylpyrrolidone (NMP) solvent as binders. The slurry was then stirred for 3 h and subsequently casted onto Al foils. After drying at 110 °C for 10 h under vacuum, the foils were cut into cathode electrodes with 10 mm diameter and assembled into CR2032 coin cells with lithium metal foil anodes, Celgard 2400 separators and 1 M $LiPF_6$ electrolyte with solvent containing equal volume of ethylene carbonate (EC), ethyl methyl carbonate (EMC), and dimethyl carbonate (DMC) in an argon-filled glovebox.

Galvanostatic discharge-charge tests were performed 12 h after battery assembly in a NEWARE battery cycler with voltage ranging from 2.7 to 4.5V compared to Li^+/Li. All batteries were tested under a series of charge-discharge rate (0.1C, 0.2C, 0.5C, 1C, 2C, 5C) at room temperature. Electrochemical impedance spectroscopy (EIS) was performed using a CHI604E electrochemical workstation with voltage amplitude of 10 mV in the frequency range of 0.1 Hz–100 kHz.

3. Results and discussion

3.1. Electrochemical performance

In order to reveal the effect of heat treatment on electrochemical properties of NCM811, the cycling and rate capability were tested by assembling coin cells with corresponding heat-treated NCM811 samples as cathodes. In cycling test, active mass loading on the Al foils were 0.98, 0.99, 0.93, 1.02 and 1.04 mg for the as-prepared sample and samples treated at 400, 600, 700 and 800 °C, respectively. As for rate performance test, the active mass were 0.93, 1.04, 1.10, 1.11 and 1.06 mg for as-prepared, 400°C-treated, 600°C-treated, 700°C-treated and 800°C-treated samples. The 1st charge-discharge profiles are shown in Fig. 1a. It can be seen that initial charge and discharge capacity of pristine (218.9 mAh·g^{-1}) and 400°C-treated sample (221.0 mAh·g^{-1}) were almost equal at the rate of 0.1C, while samples treated at 600 °C and 700 °C displayed poorer initial capacity of 211.8 and 201.4 mAh·g^{-1}, respectively. With further increase in heat treatment temperature up to 800 °C, NCM811 sample exhibit poor electrochemical performance as indicated by low coulombic efficiency (42.24%) and much lower capacity (86.6 mAh·g^{-1}). After activation at 0.1C for 3 cycles, long-cycle testing was carried out. Fig. 1b shows the efficiency and discharge capacity of tested samples at 1C in 200 cycles. Among all cells, the one assembled with 400°C-treated NCM811 cathode exhibits the best cycle stability and high coulombic efficiency. For the 600°C-treated sample, capacity of the cell dropped rapidly compared with that of the pristine sample. As for the 700°C-treated sample, it is obvious that the cycling stability was very poor, resulting in great capacity loss of the cell. After the sample was heat-treated at 800 °C, the significant structure changes resulted in nearly no electrochemical activity of the cathode material. Moreover, rate performance shows the same tendency as reflected from the cycling test. In Fig. 1c, the 400°C-treated sample displayed the best capacity, especially when it was charged and discharged at high rate (~132.5 mAh·g^{-1} at 5C). The cell assembled with 600°C-treated cathode also showed optimized high-rate performance. Additionally, it exhibited a slow activation stage in the low rate stage, suggesting that the particle surface was damaged and it became a barrier to block the diffusion of lithium from the bulk to the electrolyte [30,31]. The reason for enhanced rate performance of 400°C-treated and 600°C-treated NCM811 can be attributed to the altered surface structure and the increased layer distance, which will be beneficial for quick Li^+

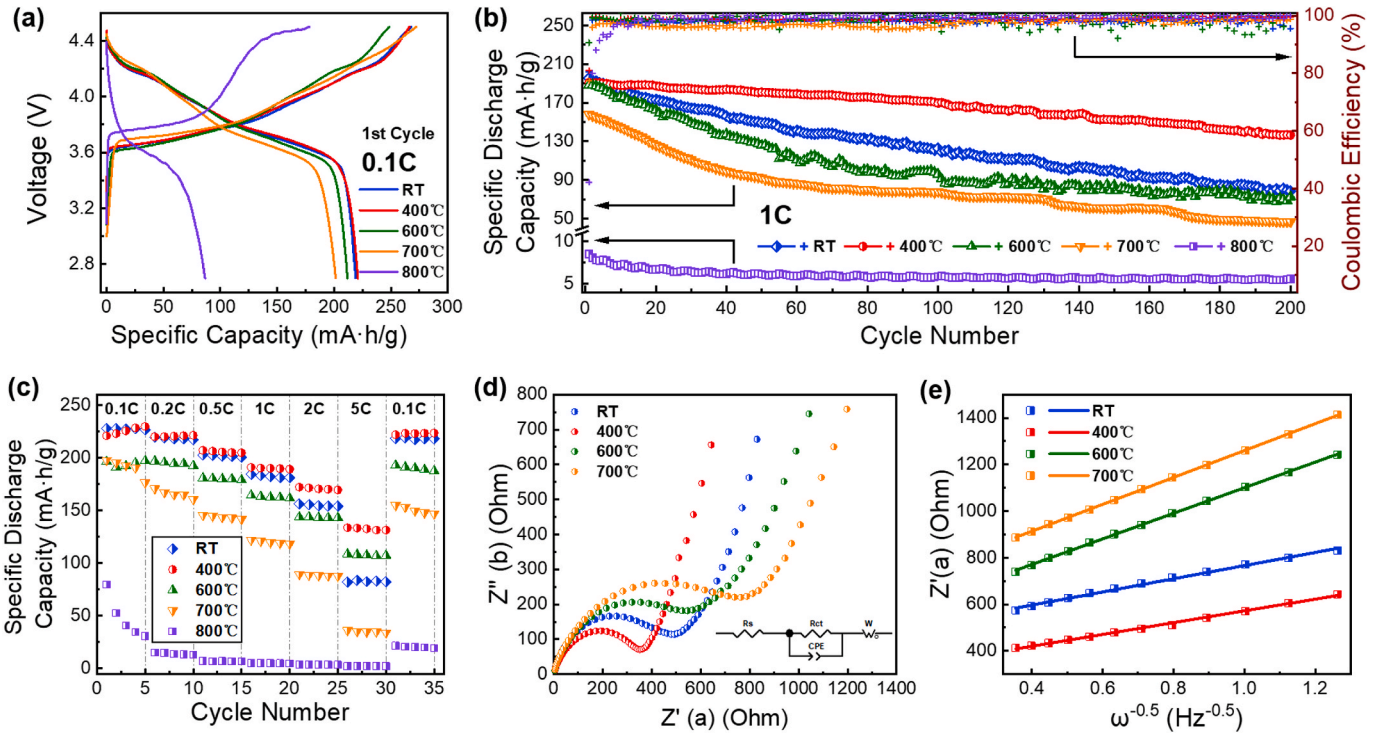

Fig. 1. Electrochemical properties of half cells with NCM811 cathodes treated from RT to 800 °C. (a) 1st charge/discharge curves at 0.1C, (b) cycling performance at 1C, (c) rate performance at 0.1C, 0.2C, 0.5C, 1C, 2C and 5C, (d) Nyquist plots of NCM811 samples before cycling, (e) Z′-$\omega^{-0.5}$ diagram. All cells were tested between 2.7 and 4.5 V at 25 °C.

intercalation and deintercalation, as further discussed below.

To compare the diffusion behavior of Li^+ in NCM811 samples under different heat treatment conditions, EIS spectrum of samples after the 1st cycle was obtained and fitted by the circuit model shown in Fig. 1d. As demonstrated by EIS spectrum, each sample exhibits a low-frequency tail associated with Li^+ diffusion and a high-frequency semi-circle related to the surface charge transfer. Thus, the model shown in Fig. 1d was selected to fit the spectrum, with the impedance Z written as

$$Z = R_s + R_{ct} + \sigma\omega^{-\frac{1}{2}}. \quad (1)$$

Here, R_s and R_{ct} represent the resistance of electrolyte and the charge transfer resistance respectively [32,33]. Additionally, at low-frequency range, slope of the real part of impedance against to the inverse of the square root of frequency is called the Warburg coefficient σ [34,35]. The Z'-$\omega^{-0.5}$ diagram was plotted in Fig. 1e. Based on the Warburg coefficient, diffusion coefficient of Li^+, i.e. D_{Li}^+, can be deduced by

$$D_{Li^+} = \frac{R^2T^2}{2A^2n^4F^4c^2\sigma^2}. \quad (2)$$

Both resistance value and diffusion parameters of Li^+ were summarized in Table S1. Obviously, the 400°C-treated sample displayed the lowest R_{ct} of 289.6 Ω and the highest D_{Li}^+ of 1.2×10^{-12} cm^2 s^{-1} due to the optimal crystal structure for Li^+ transport. The diffusion coefficient of Li^+ in 400°C-treated sample is even higher than that in pristine sample. In contrast, the 600°C-treated sample shows higher resistance and lower diffusion coefficient because of the damage of particle surface. The microstructure of NCM811 further deteriorated for the 700°C-treated one. To conclude, 400°C-treated NCM811 exhibited excellent cycling stability as well as the rate performance.

3.2. Effect of heat treatment on modification of surface

In order to get insight into the intrinsic mechanism concerning the improvement of electrochemical properties of heat treated NCM811 samples. We first investigate the effect of heat treatment on modification of surface of samples. The SEM images of as-prepared, 400°C-treated and 600°C-treated NCM811 particles are shown in Fig. 2a–c. At room temperature, the as-prepared NCM811 cathode particles have sphere-like morphology with diameter of about 3 μm in Fig. 2a. When treated at 400 °C, NCM811 samples showed similar fine spherical morphology (Fig. 2b) to that at room temperature (Fig. 2a). However, when heat-treated temperature reached higher than 600 °C, the gradual fracture of secondary particles was clearly observed. The collapse of secondary particles, which introduced more defects on the surface, was shown to have negative effect on the structural stability of particles [30] in agreement with our observations in this work. As for the samples treated at even higher temperature, particles with smooth contour gradually changed to those with sharp edges, implying the transformation of crystal structure in this temperature interval and leading to the failure of cathode materials (Figs. S1b–e). During this stage, particles of the new phase continued growing up and finally replaced original particles, resulting in polyhedron-like morphology of the sample treated at 1000 °C in Fig. S1e.

The evolution of surface state as discussed above was confirmed by the XPS spectra in Fig. 2d–f, with fitted results listed in Table S2. From the O 1s spectra in Fig. 2a, two distinct peaks representing different species were observed clearly. According to previous research [24], the peak around 531 eV is attributed to metal carbonate (i.e. Li_2CO_3 and transition metal carbonate) and another peak around 528 eV originated from metal oxide (i.e. the oxygen in the layered phase lattice). The intensity of spectra reflects the amount of these species on the particle surface. Once the treated temperature increased, the intensity of metal carbonate decreased compared to metal oxide, indicating that the Li_2CO_3 on particle surface decomposed. The decomposition of Li_2CO_3 results in the increase of exposure area of NCM811 particles, leading to the strengthening of metal oxide signals. From the change of peak intensity, it can be inferred that the particle surface became much cleaner, which is beneficial for Li^+ diffusion to enhance the cycling stability and rate performance, especially under high rate. On the other hand, apparently, the higher temperature also accelerates the surface reconstruction process, which results in degradation of cycling and rate performance of layered materials. In the samples treated at high temperature above 600 °C, the transition metal cations, especially Ni^{2+}, could concentrate on the surface and thus increase the Li/Ni disordering accordingly, impeding Li^+ diffusion. Indeed, the Ni 2p spectra shown in Fig. 2e reveal this effect. Taking the peak around 855 eV as an example, it is composed of two separate peaks representing two different valence states [24,36]. The left peak corresponds to Ni^{3+} while the right one corresponds to Ni^{2+}. When temperature of 400 °C was used, only slight change in the peak intensity was observed. In contrast, the amount of Ni^{2+} increased significantly in 600°C-treated sample compared to the samples treated at lower temperature. These XPS spectra clearly illustrated that the concentration of Ni^{2+} increases on the surface with

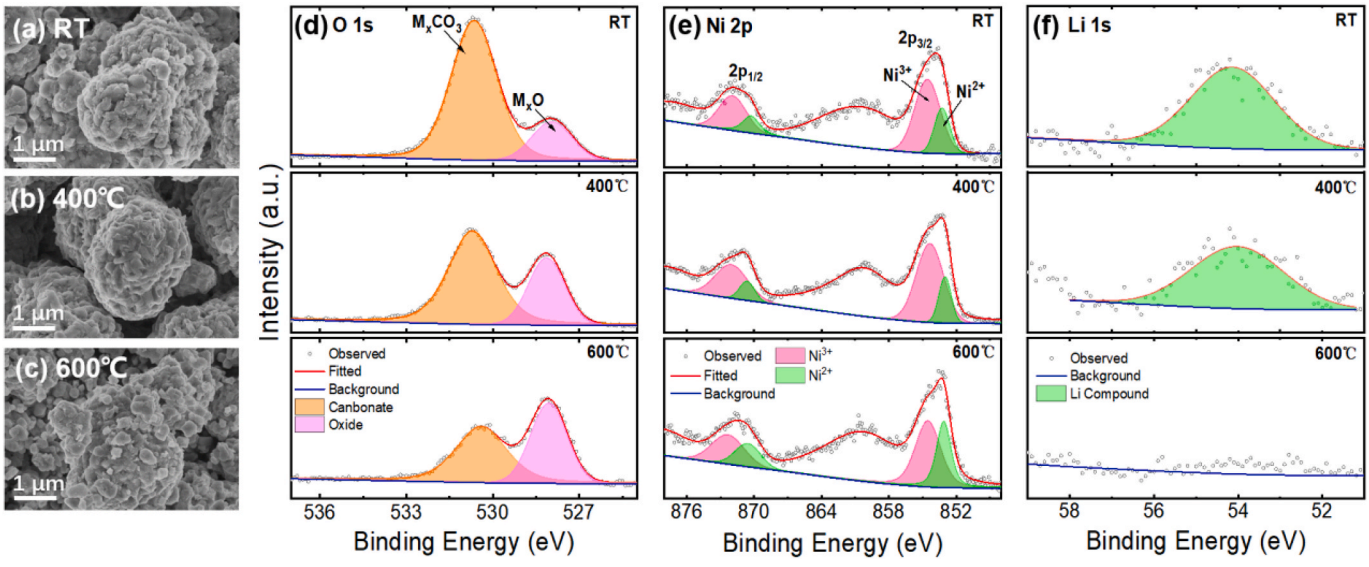

Fig. 2. Surface morphology SEM images of secondary particles treated at (a) RT, (b) 400 °C and (c) 600 °C and XPS patterns of (d) O 1s, (e) Ni 2p and (f) Li 1s for as-prepared NCM811 cathode treated at 600 °C, 400 °C and RT, respectively.

increasing heat-treatment temperature. Moreover, as shown in Fig. 2f, the Li 1s peak around 54.9 eV disappeared at 600 °C, which also hints vacancies on the surface. Based on the Ni 2p and Li 1s spectra, it is reasonable to conclude that Li/Ni disordering concentrated on the surface particle, which hinders the diffusion of Li^+ from bulk to electrolyte, increases the impedance and results in poorer capacity under low rate. To sum up, heat-treatment of NCM811 sample at low temperature is beneficial for electrochemical performance due to the surface optimization, while heat-treatment at high temperature is detrimental to the particle surface of NCM811 by introducing more Li/Ni disordering due to the accumulation of Ni^{2+} and Li^+ loss on the surface.

3.3. Bulk structure instability induced by high-temperature treatment

Generally, heat treatment process can modify not only surface structure but also inner structure of materials. In order to acquire information on structural evolution during heat treatment, especially the change of lattice parameters and antisite defects, neutron diffraction was used to investigate the heating process owing to its strong ability to distinguish lithium and transition metal elements in NCM811. Moreover, Rietveld refinement technique was applied to extract accurate crystallographic information from the NPD patterns. *In-situ* NPD patterns and refinement results are given in Fig. 3a and Fig. S2a. A rhombohedral $LiNiO_2$ structural model [36] (denoted as L, shown in Fig. 3c) with $R\bar{3}m$ space group (PDF #09–0063) was chosen to fit the diffraction pattern of the sample at RT and 400 °C. In this model (Table S3), most Li atoms occupy 3*a* site while transition metal atoms and oxygen atoms occupy 3*b* and 6*c* sites, respectively. During the refinement possible Li/Ni disordering was also taken into account, i.e. Li and Ni atoms were both allowed to partially occupy both 3*b* and 3*a* sites. As shown in Fig. S2a, the two NPD patterns can be described properly by rhombohedral structural model and no extra peaks appear in the patterns, which confirms the stability of the ordered layered structure of NCM811 in the relatively low temperature range.

Once the temperature reached higher than 700 °C, reflections of the second phase appeared at about 34.63°, 69.48°, 73.05°, etc. By indexing the pattern at 1000 °C, it is found that only Li_2O (denoted as LO, shown in Fig. 3e, PDF #12–0254) can fit all the reflections of the second phase. Hence, based on the NPD pattern of the sample at 700 °C, it can be concluded that layered NCM811 was delithiated at high temperature and lithium precipitated in form of lithium oxide, indicating the beginning of the failure process of layered cathodes.

By comparing the intensity of diffraction peaks of Li_2O at higher temperature, it is obvious that amount of Li_2O increased with the temperature, due to the instability of layered structure. As a result, at 700 °C, layered rhombohedral phase of NCM811 started to decompose into an electrochemical-inactive cubic rock-salt phase due to the lowering amount of lithium at 3*a* site. The decrease of (003) and (101) reflection intensity of layered phase at 19.43° and 38.00° indicates the disappearance of layered structure. Finally, accompanied with the collapse of rhombohedral phase, reflections of sample merged into the $Fm\bar{3}m$ rock-salt structure [24] (denoted as R, shown in Fig. 3d). The rock-salt structure with nominal formula MO (M = Li, Ni, Co, Mn) can be described by using a cubic structure model (PDF #47–1049) in which transition metal and remaining lithium atoms occupy 4*a* site and oxygen atoms are at 4*b* site (Table S3). Therefore, as Li_2O precipitated from the bulk, NCM811 transformed into rock-salt phase, leaving small amount of disordered layered phase. And after the temperature was higher than 800 °C, the disappearance of (003) and (101) reflections indicated that the rhombohedral to cubic phase transformation was finished completely.

The *in-situ* neutron diffraction results clearly reveal the structural phase transition of NCM811 upon heating. To further investigate the effect of heat treatment and reversibility of the transformation, *ex-situ* NPD experiments were carried out. Fig. 3b shows the *ex-situ* patterns of series of NCM811 samples after heat-treated at different temperatures. Similar to *in-situ* counterparts, the *ex-situ* samples exhibited similar evolution process from layered structure to rock-salt type induced by

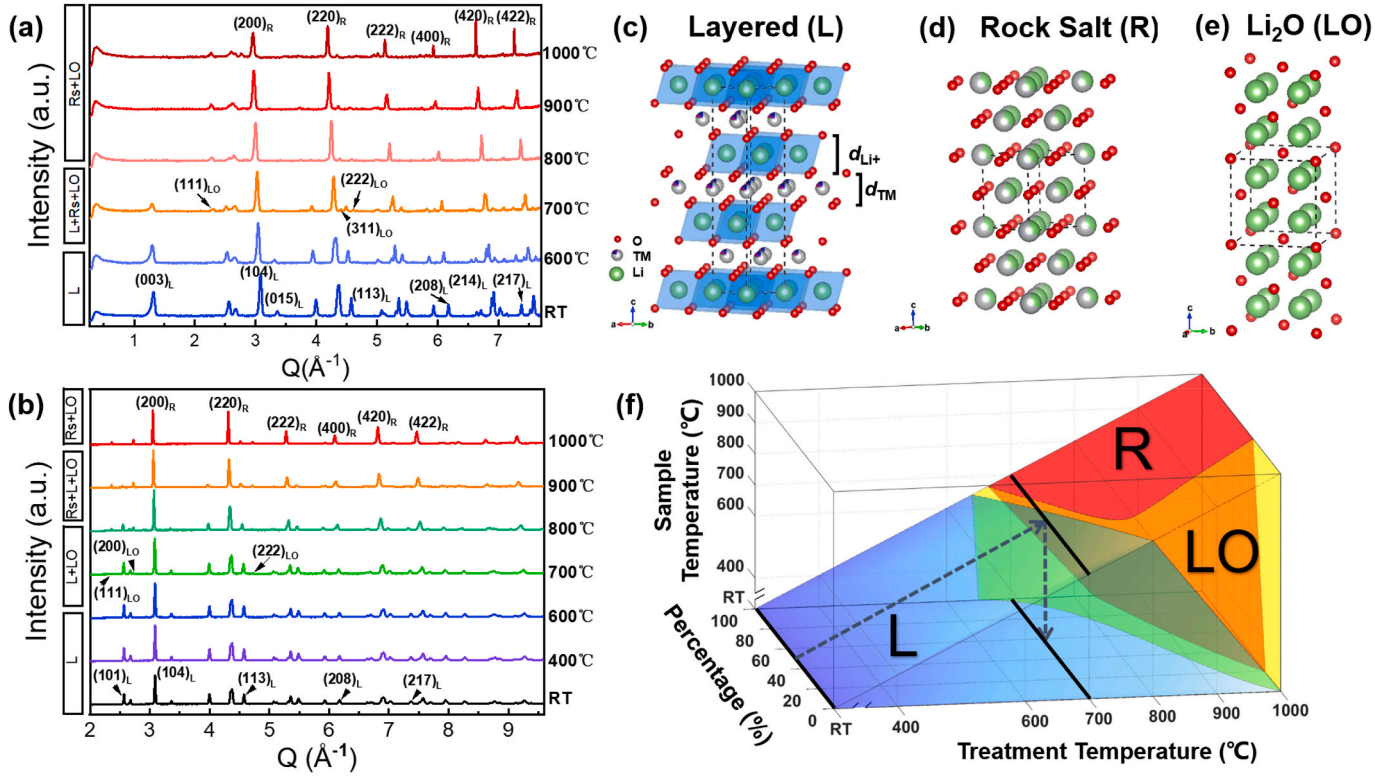

Fig. 3. (a) *In-situ* and (b) *Ex-situ* NPD patterns of NCM811 cathode materials treated at different temperatures. Crystal structure of (c) layered phase, (d) rock salt and (e) Li_2O. (f) 3D phase diagram of NCM811 correlates the phase percent at different temperatures.

delithiation with increasing heat-treated temperature. By applying the same analysis procedures for the *in-situ* NPD patterns, the phase composition as well as crystallographic information of individual phase were also extracted based on structural refinements. Refinement results are given in Fig. S2b.

According to *ex-situ* NPD refinement results, considerable amount of Li_2O was observed in sample heat-treated at high temperature. It is worth noting that although Li_2O is prone to react with CO_2 and H_2O in the air and generate Li_2CO_3 and LiOH compounds, the kinetics of these reactions are relatively slow. Based on the XRD measurements shown in Fig. S3, it will take about one week to generate detectable amount of hydrate and carbonate from Li_2O. Given that NPD experiment was carried out one day after the heat treatment and all samples were preserved carefully, it was reasonable to detect only Li_2O from the bulk sample rather than Li_2CO_3 or LiOH.

It was previously reported that the thermally induced phase transition from the layered to the spinel-like structure took place in layered cathode material under high delithiated state. Such phase transition is difficult to observe if the lithium content x of layered oxide cathode Li_xMO_2 is larger than 0.6 as the critical point shifts to higher temperature with the increase of lithium content x [37]. Among all the NCM811 samples studied in the present works, spinel-like structure [38] (space group $Fd\bar{3}m$, PDF #35–0782) was not observed even in the 900°C-treated NCM811, which consists of three different phases. It can be attributed to the lack of vacancies at the 3*a* site where Li^+ occupies. According to previous reports, layered-to-spinel-like transformation requires two steps-the migration of Li^+ from 3*a* site to 6*c* site and the transfer of transition metal ions from 3*b* site to 3*a* site [39,40]. Both steps are less possible to occur when Li^+ is fully occupied at 3*a* site since the migration barrier could be much higher than that in the delithiated state. When the temperature is high enough for Li_2O to precipitate from the bulk, Li^+ tends to escape from the lattice rather than migrate to another site. As a result, the layered structure directly transforms to rock-salt structure, without the appearance of spinel-like structure. In summary, the result of NPD experiments reveals the whole structural transformation process of NCM811, in which the intrinsic mechanism is associated with the delithiation of material with increasing temperature.

By comparing the two sets of NPD patterns, it is found that the phase transition temperatures are remarkably different between *in-situ* and *ex-situ* heating processes. For the *in-situ* sample, layered structure phase transforms into rock salt at 700 °C (Fig. 3a) with simultaneous appearance of lithium oxide, while the corresponding *ex-situ* sample maintain its original structure (Fig. 3b). As mentioned above, peaks of rhombohedral phase disappeared in the *in-situ* patterns once temperature was higher than 800 °C, indicating the complete phase transition in NCM811. However, according to the *ex-situ* experiment, layered NCM811 did not start to transform into rock-salt phase unless it was heat-treated at 900 °C. From observed phase transition phenomenon, it is safe to infer that NCM811 lost the lithium ion at 3*a* site and transformed into the rock-salt structure during heating stage, subsequently NCM811 re-lithiated and reversed to layered structure during cooling process. In inverse direction of the decomposition, solid state reaction between rock salt and Li_2O is also able to occur under high temperature, leading to the formation of layered structure phase. Therefore, this evolution process involves a chemical equilibrium between decomposition and formation of NCM811. During heating, the decomposition rate is faster than the formation rate, resulting in the forward movement of the equilibrium and the increase of rock-salt phase. Upon cooling, the formation rate is faster than decomposition rate, inducing the inverse movement of chemical equilibrium as well as the recovery of layered structure. However, at low temperature, reaction rate is relatively low. The slow recovery finally leads to a partial reversible structural evolution process of NCM811.

Phase fraction of NCM811 during heating (*in-situ*) and after heating (*ex-situ*) was also determined quantitatively based on the refinement results listed in Table S4 and Table S5. To correlate phase diagram obtained by two sets of NPD experiments, we created a 3D phase diagram as shown in Fig. 3f to directly express the phase evolution process of heat-treated NCM811 sample. In the diagram, the transversal axis represents the heat-treating condition of a specific sample. And the vertical axis is the real temperature of a sample which is being heat-treated. The longitudinal axis gives the phase composition of a sample at the given state. Therefore, the *in-situ* data reflects the states where the temperature reaches the selected heat-treated point, while the *ex-situ* data is those where it returns to room temperature, i.e., the *ex-situ* NPD patterns can be considered as the projection of *in-situ* patterns by connecting corresponding temperature points of two sets of patterns.

As illustrated in the 3D phase diagram in Fig. 3f, the thermally-induced phase transition of NCM811 cathode from layered to rock-salt structure is partially reversible, resulting in the shift of phase boundary from high temperature range in *in-situ* case to low temperature range in *ex-situ* case. Overall, the structural evolution process of NCM811 can be summarized as the following three stages:

$$(Li_{1-\delta}Ni_{\delta})^{3a}(Li_{\delta}Ni_{0.8-\delta}Co_{0.1}Mn_{0.1})^{3b}O_2^{6c} \overset{<700^{\circ}C}{\leftrightarrow} (Li_{1-\delta-\Delta}Ni_{\delta+\Delta})^{3a}(Li_{\delta+\Delta}Ni_{0.8-\delta-\Delta}Co_{0.1}Mn_{0.1})^{3b}O_2^{6c}. \quad (3)$$

$$(Li_{1-\delta}Ni_{\delta})^{3a}(Li_{\delta}Ni_{0.8-\delta}Co_{0.1}Mn_{0.1})^{3b}O_2^{6c} \overset{700\sim900^{\circ}C}{\leftrightarrow} (Li_{1-\delta-\Delta-2x}Ni_{\delta+\Delta})^{3a}(Li_{\delta+\Delta}Ni_{0.8-\delta-\Delta}Co_{0.1}Mn_{0.1})^{3b}O_{2-x-2y}^{6c} + xLi_2O + yO_2\uparrow. \quad (4)$$

$$(Li_{1-\delta}Ni_{\delta})^{3a}(Li_{\delta}Ni_{0.8-\delta}Co_{0.1}Mn_{0.1})^{3b}O_2^{6c} \overset{>900^{\circ}C}{\leftrightarrow} (Li_{2x}Ni_{0.8}Co_{0.1}Mn_{0.1})O_{1+x+2y} + (0.5-x)Li_2O + (0.25-y)O_2\uparrow. \quad (5)$$

Taking the 700°C-treated NCM811 sample as an example, according to the marked route in Fig. 3f and the corresponding expanded 2D phase diagram in Fig. S4, it crystallized in layered structure at room temperature as shown in Fig. 3c. When sample was heated to 600 °C, the rhombohedral structure of NCM811 persisted although Li/Ni disordering defects accumulated on the surface of particles. As temperature increases further to 700 °C, certain amount of Li_2O precipitates from layered structure. This process can be associated with the continuous diffusion of Li^+ from the inner region to the surface of particles [24]. Therefore, it is reasonable to presume that layered phase with low Li^+ decomposed into rock-salt phase on the particle surface firstly, while the Li ions in layered phase continuously migrate from inner region to the surface. This hypothesis could be verified by TEM images of cathode samples, as discussed below. In brief, the decomposition of layered structure lead to the emergence of rock salt at the temperatures higher than 700 °C. During the cooling procedure, NCM811 sample with mixed layered, rock salt and Li_2O phases partially recovers back to its original layered structure through reconstruction and reaction with the precipitated Li_2O. However, recovery process is not fully reversible, resulting in poor electrochemical performance in 700°C-treated NCM811 sample.

TEM images provide evidence for the phase transformation scenario discussed above. Fig. 4a–c shows the high-resolution TEM images of the 1000°C-treated, 900°C-treated and 800°C-treated NCM811 particles, respectively. The atomic arrangements of layered and rock-salt structure in real space along several zone axes are illustrated in Fig. 4d–e. Values of the interplanar spacing obtained from TEM images are given in Table S7, which is in good agreement with the values that obtained from Rietveld refinement based on the NPD data. It is obvious that both the surface and the inner region of 800°C-treated particles were layered phase, as demonstrated in Fig. 4c. After heat treatment at 900 °C, the surface structure of particle is observed to be rock-salt type (Fig. 4b), confirming that the layer to rock-salt phase transition is induced by substantial delithiation on the surface of particles. Clearly, the 1000°C-treated sample possesses only the rock-salt phase both on the surface and in the inner part of particles (Fig. 4a). Moreover, it is found that *d*-spacing of (003) plane in layered phase increased gradually with

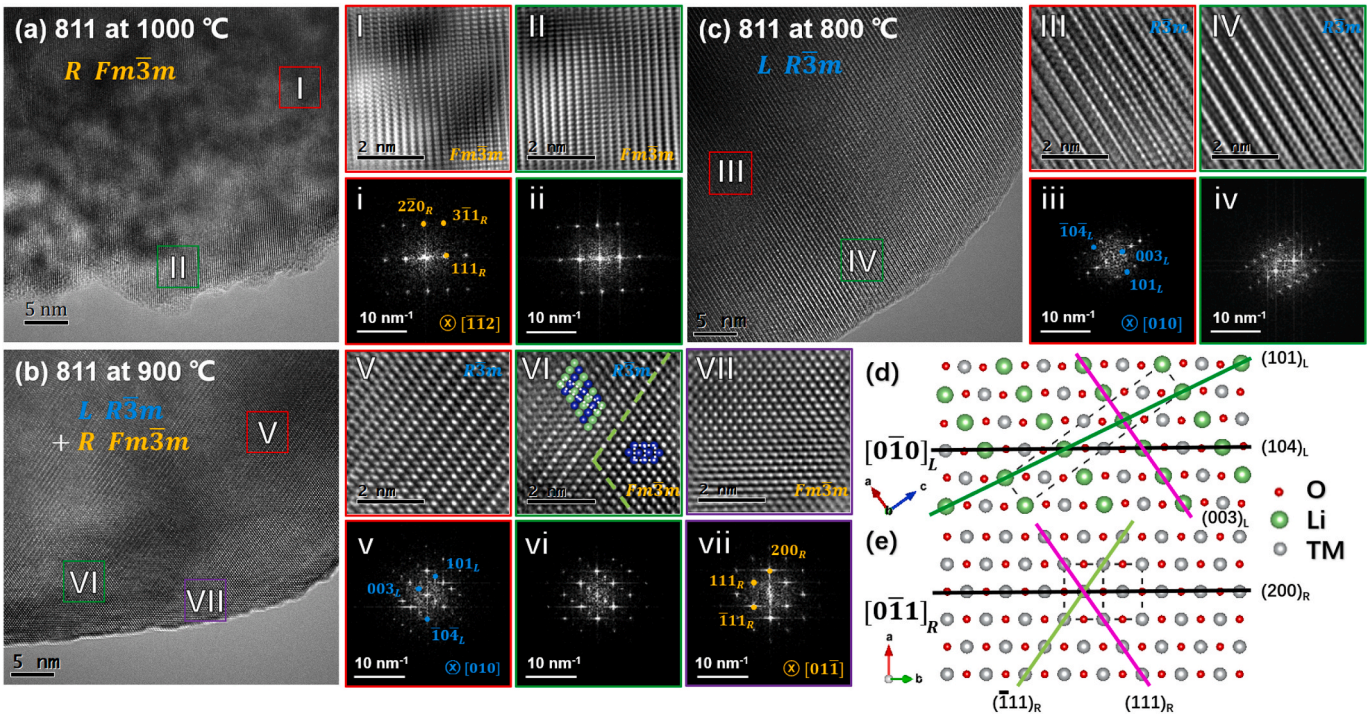

Fig. 4. TEM images of NCM811 particles heat-treated at (a) 1000 °C, (b) 900 °C and (c) 800 °C. Images with lower-case Roman numerals are the FFT mappings of the corresponding square regions marked in the TEM photographs. And those with upper-case numerals are the IFFT images of the corresponding FFT graphs. Atomic arrangement at (d) [0$\bar{1}$0] zone axis of layered phase and (e) [0$\bar{1}$1] zone axis of rock salt are also provided.

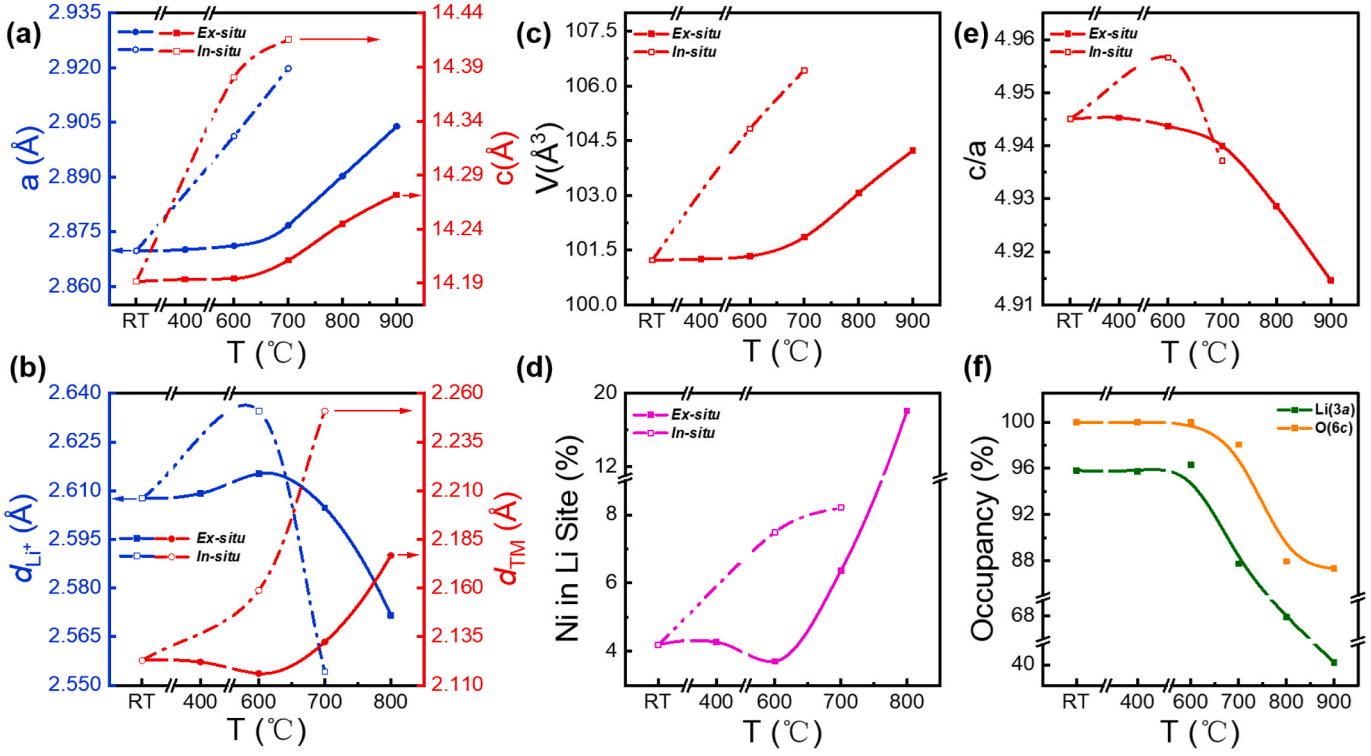

Fig. 5. (a) Lattice parameters, (b) Li^+ slab and TM slab spacing, (c) volume change, (d) Li/Ni disordering ratio, (e) ratio of c and a and (f) occupancy of Li at 3*a* site and O at 6*c* site of NCM811 layered phase obtained from the refined *Ex-situ* and *In-situ* neutron diffraction patterns. The d-spacings of Li and TM slabs are obtained by: $0.5c = 1.5d^{+}_{Li}+1.5d_{TM}$, and $z_O = 2.5d^{+}_{Li}+2d_{TM}$, in which z_O is the position of O on the *c* axis.

increasing heat treatment temperature, indicating the irreversible expansion of lattice in the heat-treated samples. The combination of the TEM and NPD results provides a clear picture of the structural evolution process of NCM811 at both local and average level.

To further systematically illustrate details of the thermal-induced structural evolution process of NCM811, refinement results from *in-situ* and *ex-situ* NPD experiments were combined. Fig. 5 shows the variation of several important crystallographic parameters as a function of temperature, while the corresponding refinement results are given in Table S4 and Table S5. The agreement factors are also provided in Table S6. In Fig. 5a, the temperature dependence of lattice parameters *a* and *c* in layered rhombohedral phase is plotted. For the *in-situ* NPD results, both lattice parameters *a* and *c* increased with increasing temperature due to thermal expansion. However, the variations of *a* and *c* after cooling to room temperature exhibit different behaviors as demonstrated by the *ex-situ* NPD results. When the heat treatment temperature is lower than 600 °C, lattice parameters of the samples are almost constant, indicating the recovery of thermally-induced strain in the low temperature region. For the samples treated above 600 °C, lattice parameters increased significantly, reflecting irreversible spacing change in the layered structure. To get insight, the thicknesses of Li^+ slabs (d_{Li}^+) and transition metal (TM) slabs (d_{TM}) were obtained from refinement data and shown in Fig. 5b. After cooling, the thickness of TM slabs shrinks for T < 600 °C and expands for T > 600 °C, while the Li^+ slabs distance exhibits the opposite tendency. Variation of volume of the unit cell is shown in Fig. 5c, which exhibits similar trend as the corresponding lattice parameters. The variation of slab thickness as well as lattice parameters in the *in-situ* NPD results is attributed to the thermal expansion of samples. It is obvious that lattice parameters increased with the raise of temperature, except the Li-slab thickness at 700 °C. According to the previous discussion, Li_2O precipitated from the bulk when temperature is higher than 700 °C. The rapid loss of Li_2O would lead to the collapse of Li^+ layer. As a consequence, Li-slab distance shrank significantly.

The evolution of the crystallographic parameters in the *ex-situ* NPD results could be explained by considering the change of Li/Ni disordering in the bulk of the materials. It is known that Li/Ni disordering inevitably exists in high-Ni layered oxides due to close radius of Li^+ and Ni^{2+} ions as well as magnetic interactions [21]. As shown in Fig. 5d, cation disordering in layered structure phase was also influenced by heat treatment process. The Li/Ni disordering ratio could be defined as the fraction of Ni^{2+} at 3*a* site, which should be occupied by Li^+ in the ideal fully ordered structure. In Fig. 5d, the Li/Ni disordering ratio at room temperature is the intrinsic disordering ratio δ in equations (3)–(5) of the as-prepared NCM811 cathodes, which is around 4.19%. According to the *in-situ* results, during heating, Li/Ni disordering ratio in layered structure phase increased monotonically with increasing temperature because temperature allows cations to overcome energy barrier and migrate to an adjacent cation layer. As indicated by the *ex-situ* results, the Li/Ni disordering ratio in heat-treated samples decreased during cooling process. The Li/Ni disordering ratio decreased from 7.49% to 3.71% in 600°C-treated sample, while it decreased from 8.22% to 6.36% in 700°C-treated sample. As expected, the decreasing tendency was weakened with the raise of heat treatment temperature. It is also clear that the 600°C-treated sample possesses the lowest Li/Ni disordering ratio among all samples. However, the poor structural homogeneity in particles, especially the concentration of Li/Ni disordering on the surface impedes Li^+ diffusion and electron conduction in 600°C-treated sample. Furthermore, the lowest Li/Ni disordering represents the highest amount of Li^+ in the Li^+ slabs. Considering that the charge number of Li^+ is 1, the Coulomb force between Li^+ and oxygen is relatively low compared to that between TM ions and oxygen. Then the thickness of Li^+ slabs increased with the decrease of Li/Ni disordering due to the reduction of coulomb interaction to the oxygen. The shrinkage of TM slabs could be also explained by the decrease in Li/Ni disordering. As for the 700°C- and 800°C-treated samples, the Li/Ni disordering increased sharply, indicating large amount of Ni^{2+} existing in the Li^+ slabs, which greatly strengthened the repulsive force between the adjacent cations and led to significant increase of lattice parameter *a* and *c* as well as d_{TM}. Both the stronger coulomb interaction and the Li/O loss lead to the shrinkage of Li^+ slabs. In addition, lithium-loss-induced phase transition took place in samples during heating process. As a consequence, less chemically active substance exists in the cathode and the electrochemical performance becomes worse as expected.

Another prominent feature is the change of the *c/a* ratio as shown in Fig. 5e, which hints the gradual collapse of the layered structure. It is reported that a well-defined rhombohedral structure of $LiNi_xCo_yMn_zO_2$ should satisfy the relation $c/a > 4.9$ [41,42]. Although all samples in the *ex-situ* experiment possess the *c/a* ratio larger than 4.9, the sharp negative trend indicates the growing deviation of sample structures from the ideal rhombohedral type due to the Li/O loss and the increasing Li/Ni disordering ratio. The decrease of *c/a* ratio is also observed in the *in-situ* experiment at 700 °C, which corresponds to the decomposition of layered phase. Among all samples, maximum of the *c/a* ratio, 4.9453, is found in the 400°C-treated sample, implying its crystal structure is the closest to the ideal, which leads to the best electrochemical performance of NCM811 cathode. Additionally, existence of lithium and oxygen vacancies was revealed by the sharp decrease trend of Li (3*a*) and O (6*c*) occupancy rate in Fig. 5f, which is consistent with the discussion above. In summary, the changes of crystallographic parameters are associated with the precipitation of Li_2O as well as the increase of Li/Ni disordering during heating process. The change of bulk structure, accompanied with the change of surface structure, contributes to the optimization of electrochemical performance in NCM811 cathode materials after heat treatment process.

4. Conclusions

In this work, *in-situ* NPD, *ex-situ* NPD and FE-TEM methods were combined to systematically investigate the thermal-induced structural evolution in NCM811 cathode material. When treated at 400 °C, NCM811 is able to recover from the disordered structure with optimized surface morphology, thus improving electrochemical behavior. Herein, reheating at low temperature could be a simple but useful way to enhance the properties of layered cathode materials. If heat treatment temperature is higher than 700 °C, layered rhombohedral phase transforms into cubic rock salt due to delithiation and Li/Ni disordering accumulation. This work provides deeper understanding about the thermal stability of high-Ni layered cathode materials and offers a strategy to design improved heat treatment process to produce better cathode materials.

CRediT authorship contribution statement

Zhongyuan Huang: Methodology, Formal analysis, Writing - original draft, Visualization. **Mihai Chu:** Methodology, Formal analysis. **Rui Wang:** Methodology, Formal analysis. **Weiming Zhu:** Methodology, Formal analysis. **Wenguang Zhao:** Investigation. **Chaoqi Wang:** Validation, Writing - review & editing. **Yanjun Zhang:** Formal analysis. **Lunhua He:** Investigation, Resources. **Jie Chen:** Investigation. **Sihao Deng:** Investigation. **Longwei Mei:** Investigation. **Wang Hay Kan:** Formal analysis, Investigation. **Maxim Avdeev:** Investigation, Resources. **Feng Pan:** Formal analysis, Resources. **Yinguo Xiao:** Conceptualization, Writing - review & editing, Supervision.

Declaration of competing interest

The authors declare that they have no known competing financial interests or personal relationships that could have appeared to influence the work reported in this paper.

Acknowledgement

The research was financially supported by National Key R&D Program of China (2017YFB0701900), Guangdong Basic and Applied Basic Research Foundation (No. 2019A1515012060, 2019B1515120028, 2017A030313021 and 2016A030313129), National Natural Science Foundation of China (No. 11805034, 11805033, 21704105 and U1930102) and Youth Innovation Promotion Association CAS (Grant No. 2017023). The Authors appreciate the beam time at GPPD granted from China Spallation Neutron Source (CSNS) and the beam time at ECHIDNA granted from Australian Centre for Neutron Scattering (ACNS) in ANSTO.

Appendix A. Supplementary data

Supplementary data to this article can be found online at https://doi.org/10.1016/j.nanoen.2020.105194.

References

[1] M. Armand, J.M. Tarascon, Nature 451 (2008) 652–657.
[2] J.B. Goodenough, Y. Kim, Chem. Mater. 22 (2010) 587–603.
[3] H. Li, Z.X. Wang, L.Q. Chen, X.J. Huang, Adv. Mater. 21 (2009) 4593–4607.
[4] V. Etacheri, R. Marom, R. Elazari, G. Salitra, D. Aurbach, Energy Environ. Sci. 4 (2011) 3243–3262.
[5] J.B. Goodenough, K.S. Park, J. Am. Chem. Soc. 135 (2013) 1167–1176.
[6] J. Li, H. Liu, J. Xia, A.R. Cameron, M. Nie, G.A. Botton, J.R. Dahn, J. Electrochem. Soc. 164 (2017) A655–A665.
[7] W. Qiu, J. Xia, L. Chen, J.R. Dahn, J. Power Sources 318 (2016) 228–234.
[8] J.L. Shi, D.D. Xiao, M. Ge, X. Yu, Y. Chu, X. Huang, X.D. Zhang, Y.X. Yin, X.Q. Yang, Y.G. Guo, L. Gu, L.J. Wan, Adv. Mater. 30 (2018) 1705575.
[9] C. Lin, J. Li, C. Wang, F. Pan, Chin. J. Struct. Chem. 38 (2019) 2015–2019.
[10] Y.K. Sun, D.J. Lee, Y.J. Lee, Z. Chen, S.T. Myung, ACS Appl. Mater. Interfaces 5 (2013) 11434–11440.
[11] H. Konishi, M. Yoshikawa, T. Hirano, K. Hidaka, J. Power Sources 254 (2014) 338–344.
[12] W.S. Yoon, O. Haas, S. Muhammad, H. Kim, W. Lee, D. Kim, D.A. Fischer, C. Jaye, X.Q. Yang, M. Balasubramanian, K.W. Nam, Sci. Rep. 4 (2014) 6827.
[13] N. Yabuuchi, Y.-T. Kim, H.H. Li, Y. Shao-Horn, Chem. Mater. 20 (2008) 4936–4951.
[14] H. Konishi, T. Yuasa, M. Yoshikawa, J. Power Sources 196 (2011) 6884–6888.
[15] M. Zhang, Y. Chen, F. Pan, Y. Ren, Chin. J. Struct. Chem. 39 (2020) 26–30.
[16] D. Liu, Z. Shadike, R. Lin, K. Qian, H. Li, K. Li, S. Wang, Q. Yu, M. Liu, S. Ganapathy, X. Qin, Q.-H. Yang, M. Wagemaker, F. Kang, X.-Q. Yang, B. Li, Adv. Mater. 31 (2019) 1806620.
[17] K.W. Nam, S.M. Bak, E.Y. Hu, X.Q. Yu, Y.N. Zhou, X.J. Wang, L.J. Wu, Y.M. Zhu, K. Y. Chung, X.Q. Yang, Adv. Funct. Mater. 23 (2013) 1047–1063.
[18] C.K. Lin, Y. Piao, Y. Kan, J. Bareno, I. Bloom, Y. Ren, K. Amine, Z. Chen, ACS Appl. Mater. Interfaces 6 (2014) 12692–12697.
[19] S.M. Bak, E. Hu, Y. Zhou, X. Yu, S.D. Senanayake, S.J. Cho, K.B. Kim, K.Y. Chung, X.Q. Yang, K.W. Nam, ACS ACS Appl. Mater. Interfaces 6 (2014) 22594–22601.
[20] S.H. Lee, J.-M. Jung, J.H. Ok, C.-H. Park, J. Power Sources 195 (2010) 5049–5051.
[21] Y. Xiao, T. Liu, J. Liu, L. He, J. Chen, J. Zhang, P. Luo, H. Lu, R. Wang, W. Zhu, Z. Hu, G. Teng, C. Xin, J. Zheng, T. Liang, F. Wang, Y. Chen, Q. Huang, F. Pan, H. Chen, Nano Energy 49 (2018) 77–85.
[22] D. Wang, C. Xin, M. Zhang, J. Bai, J. Zheng, R. Kou, J.Y. Peter Ko, A. Huq, G. Zhong, C.-J. Sun, Y. Yang, Z. Chen, Y. Xiao, K. Amine, F. Pan, F. Wang, Chem. Mater. 31 (2019) 2731–2740.
[23] J. Zheng, Y. Ye, T. Liu, Y. Xiao, C. Wang, F. Wang, F. Pan, Acc. Chem. Res. 52 (2019) 2201–2209.
[24] D. Kong, M. Zhang, Y. Xiao, J. Hu, W. Zhao, L. Han, F. Pan, Nano Energy 59 (2019) 327–335.
[25] J.H. Jo, C.-H. Jo, H. Yashiro, S.-J. Kim, S.-T. Myung, J. Power Sources 313 (2016) 1–8.
[26] N.S. Nazer, V.A. Yartys, T. Azib, M. Latroche, F. Cuevas, S. Forseth, P.J.S. Vie, R. V. Denys, M.H. Sørby, B.C. Hauback, L. Arnberg, P.F. Henry, J. Power Sources 326 (2016) 93–103.
[27] J. Rodriguez-Carvajal, Physica B 192 (1993) 55–69.
[28] J. Chen, L. Kang, H. Lu, P. Luo, F. Wang, L. He, Physica B 551 (2018) 370–372.
[29] L. He, J. Chen, H. Lu, P. Luo, Y. Wu, L. Kang, J. Zhang, J. Zhang, R. Du, X. Jia, T. Liang, F. Wang, Sci. Rep. 29 (2018) 7–10.
[30] Y. Duan, L. Yang, M.-J. Zhang, Z. Chen, J. Bai, K. Amine, F. Pan, F. Wang, J. Mater. Chem. 7 (2019) 513–519.
[31] J. Zheng, P. Yan, L. Estevez, C. Wang, J.-G. Zhang, Nano Energy 49 (2018) 538–548.
[32] Y. Sun, L. Zan, Y. Zhang, Appl. Surf. Sci. 483 (2019) 270–277.
[33] C.Y. Wu, Q. Bao, Y.C. Lai, X. Liu, Y.C. Lu, H. Tao, J.G. Duh, Nano Energy 60 (2019) 784–793.
[34] Y. Liu, X. Fan, Z. Zhang, H.-H. Wu, D. Liu, A. Dou, M. Su, Q. Zhang, D. Chu, ACS Sustain. Chem. Eng. 7 (2018) 2225–2235.
[35] Q.W. Ran, H.Y. Zhao, Q. Wang, X.H. Shu, Y.Z. Hu, S. Hao, M. Wang, J.T. Liu, M. L. Zhang, H. Li, N.Y. Liu, X.Q. Liu, Electrochim. Acta 299 (2019) 971–978.
[36] R. Wang, G. Qian, T. Liu, M. Li, J. Liu, B. Zhang, W. Zhu, S. Li, W. Zhao, W. Yang, X. Ma, Z. Fu, Y. Liu, J. Yang, L. Jin, Y. Xiao, F. Pan, Nano Energy 62 (2019) 709–717.
[37] W.S. Yoon, M. Balasubramanian, X.Q. Yang, J. McBreen, J. Hanson, Electrochem. Solid State Lett. 8 (2005) A83–A86.
[38] E.Y. Hu, S.M. Bak, J. Liu, X.Q. Yu, Y.N. Zhou, S.N. Ehrlich, X.Q. Yang, K.W. Nam, Chem. Mater. 26 (2014) 1108–1118.
[39] W.H. Kan, A. Huq, A. Manthiram. Chem. Mater. 28 (2016) 1832–1837.
[40] W.H. Kan, A. Huq, A. Manthiram. Chem. Mater. 27 (2015) 7729–7733.
[41] J. Liu, W. Qiu, L. Yu, H. Zhao, T. Li, J. Alloys Compd. 449 (2008) 326–330.
[42] H. Chang, H.D. Jang, S.M. Shin, S.W. Cho, D.S. Kil, Mater. Lett. 65 (2011) 757–759.

Zhongyuan Huang received his B.S. degree in Materials Science and Engineering from University of Science and Technology Beijing, P.R. China in 2018. He is pursuing his M.S. degree in Prof. Yinguo Xiao's group at School of Advanced Materials, Peking University, P.R. China. Currently, his research interest is cathode materials synthesis control and structure characterization based on X-ray and neutron diffraction methods.

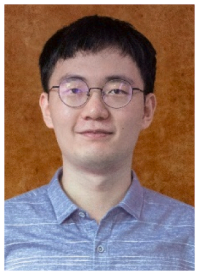

Mihai Chu received his bachelor's degree of engineering from the School of Optical and Electronic Information at Huazhong University of Science and Technology in 2017. He is currently pursuing his master degree in the School of Advanced Materials, Peking University, Shenzhen Graduate School under the supervision of Professor Yinguo Xiao. His research focuses on the synthesis of cathode materials for lithium or sodium ion batteries and the structural characterization of them including *in-situ* XRD, neutron scattering and so on.

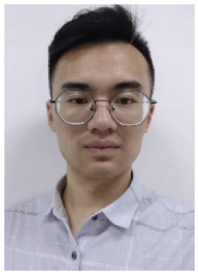

Rui Wang received his B.S. degree in Applied Physics from China University of Petroleum (East China) in 2017. He is pursuing his Ph.D. degree in the School of Advanced Materials, Peking University, China. His research interest is structural characterization for cathode materials of lithium ion battery using X-ray and neutron scattering technology.

Weiming Zhu received his B.S. degree in Materials Science and Engineering from University of Science and Technology Beijing, P.R. China in 2017. He is pursuing his M.S. degree in the School of Advanced Materials, Peking University, P.R. China. Currently, his research interests focus on thermoelectric materials.

Wenguang Zhao is an engineer in the School of Advanced Materials, Peking University Shenzhen Graduate School, China. He has over 10 years' experience in material characterization using wide range of analytical tools including XRD, XPS, SEM and TEM. His research interests mainly focus on the *Ex/in-situ* TEM and *Ex/in-situ* XRD characterization of battery materials.

Dr. Chaoqi Wang received his Ph. D. degree in Materials Science and Engineering from Xi'an Jiaotong University, in 2019. He is now working as a post-doc in Peking University Shenzhen Graduate School. His research interests focus on preparation, characterization, and properties of metal nanomaterials.

Dr. Yanjun Zhang received his Ph.D. degree in Physical Chemistry from Institute of Chemistry, Chinese Academy of Sciences in 2011. He is now working as a Research Associate in the School of Advanced Materials, Peking University Shenzhen Graduate School. His research interest is preparation, characterization and properties of electrode materials for metal-ion batteries.

Dr. Lunhua He is team leader of general purpose powder diffractometer (GPPD) at CSNS. She received her Ph.D. degree in 2002 in condensed Matter Physics from State Key Laboratory for Magnetism, Institute of Physics, Chinese Academy of Sciences, Beijing, P.R. China. She was responsible for the design and construction of GPPD. The scientific goal of GPPD is to provide a flexible and versatile powder diffractometer for a wide range of novel materials development and discovery. Her current research interests focused on the studies of neutron diffraction and scattering of magnetic materials and battery materials.

Dr. Jie Chen, associate professor, Institute of High Energy Physics, Chinese Academy of Sciences, P.R. China. He is currently an instrument scientist of general purpose powder diffractometer (GPPD) at the China Spallation Neutron Source (CSNS). He received the B.S. Degree and Ph.D. Degree both from University of Science and Technology of China, Hefei, P. R. China in 2005 and 2010, respectively. His research interests mainly include neutron diffraction/ imaging techniques, instrumentation, and applications.

Dr. Sihao Deng received his Ph.D. degree from department of Physics, Beihang University, China in 2016. He was a post-doctoral researcher from 2016 to 2019 at Karlsruhe Institute of Technology (KIT), Germany. In 2019, he joined Institute of High Energy Physics, Chinese Academy of Sciences, China as an associate professor. He is currently an instrument scientist of general purpose powder diffractometer (GPPD) at the China Spallation Neutron Source (CSNS). His current research interests is to reveal relationships between crystal (magnetic) structure and properties of materials using neutron powder diffraction technique.

Dr. Longwei Mei received his Ph.D. degree from Shanghai Institute of Applied Physics, Chinese Academy of Sciences, China, in 2013. He was an assistant research fellow from 2013 to 2014 in Shanghai Institute of Applied Physics, Chinese Academy of Sciences, China, and an assistant research fellow from 2014 to 2020 at Institute of High Energy Physics, Chinese Academy of Sciences, China. His research interests are on neutron physics, neutron optics and neutron scattering techniques.

Prof. Wang Hay Kan obtained his B.Sc. in Chemistry from HKUST in 2006. He obtained his M.Sc. and Ph.D. from University of Waterloo in 2009 and University of Calgary in 2014, respectively. He worked with other world-class scientists in UT Austin, LBNL and ANSTO. He has been an Associate Professor in China Spallation Neutron Source in 2015. Over the years, he has published 55 peer-reviewed papers, and 6 patents. Lastly, he has been awarded from International Centre for Diffraction Data - Ludo Frevel Crystallography Award (2013) and Asia-Oceania Neutron Scattering Association (AONSA) Young Research Fellowship (2017).

Maxim Avdeev received Ph.D. degree from the Rostov State University in 1999 for the work in synthesis and crystal structural studies of Na-superionic conductors. After post-doctoral position at the Argonne National Laboratory (USA), in 2005 he joined the Australian Nuclear Science and Technology Organization (ANSTO) as a full-time researcher, where he now leads Neutron Diffraction Group at the Australian Centre for Neutron Scattering. His main research interests are studies of crystal and magnetic structure of inorganic materials using X-ray and neutron diffraction and atomistic modelling.

Prof. Feng Pan, founding Dean of School of Advanced Materials, Peking University Shenzhen Graduate School, got B.S. from Dept. Chemistry, Peking University in 1985 and Ph.D. from Dept. of P&A Chemistry, University of Strathclyde, Glasgow, UK, with "Patrick D. Ritchie Prize" for the best Ph.D. in 1994. With more than a decade experience in large international incorporations, Prof. Pan has been engaged in fundamental research and product development of novel optoelectronic and energy storage materials and devices. As Chief Scientist, Prof. Pan led eight entities in Shenzhen to win 150 million RMB grant for the national new energy vehicles (power battery) innovation project since 2013.

Prof. Yinguo Xiao received his Ph.D. degree from Institute of Physics, Chinese Academy of Sciences, China in 2006. He was a postdoctoral fellow from 2007 to 2009 and a research scientist from 2009 to 2014 at Juelich Research Centre (Forschungszentrum Jülich), Germany. He became a tenured staff scientist in Juelich Research Centre since 2015. In 2017, he joined Peking University Shenzhen Graduate School, China as an associate professor. His research interests are on research and development of energy materials, magnetic materials, and characterization of complex materials using X-ray and neutron scattering techniques.